Comparison of thermal diffusion and interfacial reactions for bulk and sputtered titanium on 316L stainless steel

Jean-Marc Auger, Dominique Cotton, Corinne Nouveau, Aurélien Besnard, Frédéric Bernard, Maria-Rosa Ardigo-Besnard, Jean-Philippe Monchoux, R. Cours, Cécile Marcelot

Comparison of thermal diffusion and interfacial reactions for bulk and sputtered titanium on 316L stainless steel

J.-M. Auger [a,*], D. Cotton [a], C. Nouveau [a], A. Besnard [a], F. Bernard [b], M.-R. Ardigo-Besnard [b], J.-P. Monchoux [c], R. Cours [c], C. Marcelot [c]

[a] Arts et Metiers Institute of Technology, LaBoMaP, Université Bourgogne Franche-Comté, HESAM Université, F-71250, Cluny, France
[b] Laboratoire Interdisciplinaire Carnot de Bourgogne (ICB), UMR, 6303 CNRS, Université de Bourgogne, BP 47870, 21078, Dijon, Cedex, France
[c] Centre d'Elaboration de Matériaux et d'Etudes Structurales, Centre National de la Recherche Scientifique, Unité Propre de Recherche 8011, 29 rue J. Marvig, BP 94347, CEDEX 4, 31055, Toulouse, France

HIGHLIGHTS

- 2 steps in 316L/Ti interdiffusion: kinetics then thermodynamics controlled.
- Iron/titanium intermetallics growth kinetics not controlled by diffusion.
- Chromium diffusion blocked by Fe/Ti intermetallics, carbon trapped inside as TiC.
- Oxygen rejected from titanium by iron addition, can form surface TiO in thin films.

ARTICLE INFO

Keywords:
Titanium
Stainless steel
Diffusion couple
Intermetallics
PVD coatings

ABSTRACT

As a first step to devise a hybrid process for the production of TiC wear coatings on 316L, consisting of magnetron sputtering followed by titanium carburization, interfacial reactivity between stainless steel and titanium has to be finely understood. Systematic comparisons were carried out on diffusion couples of increasing chemical and geometrical complexity (Fe/Ti, 316L/Ti, and 316L/sputtered Ti), highlighting the formation mechanisms of interfacial structures. Transmission and scanning electron microscopy composition profiles revealed that long-range microstructures in titanium are the result of iron diffusion and oxygen impurities interactions. FeTi and Fe_2Ti intermetallics formation is first kinetically driven, then favors thermodynamic stability, leading to compositional changes during thermal cycles. Their growth is shown to be non-diffusion controlled. These compounds act as diffusion barriers for chromium, and traps for carbon, indirectly generating a complex layered structure at the interface. Differences between bulk and sputtered titanium are exclusively linked to the latter smaller scale, including destabilized diffusion fronts, and superficial TiO formation by oxygen rejection after iron diffusion.

1. Introduction

Surface modification is an old and classical way to combine multiple functionalities in a single part. Common examples include wear and corrosion protection of structural parts. The majority of methods developed to tailor surface properties can be classified as either transformative (thermo/mechanical/chemical treatments, such as nitridation [1], carburization [2] or shot peening [3]) or additive (liquid/PVD/CVD coating processes [4–6], laser cladding [7], etc.). The first category presents the advantage to natively create gradients that help maintain structures integrity, but substrate material tends to put hard limits on achievable properties. On the other hand, additive methods offer a wider range of properties combinations, but often suffer from delamination as typical failure mode, due to either mechanical (Young modulus mismatch for example) or chemical nature (metal/ceramic adhesion) incompatibility.

As the gap between the desired properties for surface and core material increased, these simple approaches have begun to show their limits. Duplex processes combining a preliminary transformative step to create an intermediate layer, before the addition of a coating providing

* Corresponding author.
E-mail address: augerj-m@laposte.net (J.-M. Auger).

final surface properties, have been successfully used for several applications. In particular, the combination of steel nitriding and nitrides deposition has seen a surge of interest in recent years [8–10]. The reverse concept (modification of a newly added surface layer, deemed a *hybrid process*), however, is a much rarer occurrence, due to the increased complexity associated with the substrate/layer interaction during transformation treatment [11].

The aim of this work is to advance the understanding of physics, chemistry and limitations involved in a hybrid process applied to industrial materials for wear applications. Selected substrate material is 316L, a stainless steel alloy commonly used for mechanical parts in difficult environments. Surface layer is TiC, chosen for its wear resistance [12], friction coefficient [13,14] and hardness [15]. This combination offers an innovative couple, adapted to recent regulations evolutions due to the use of environment and health friendly materials. Furthermore, it acts as an example of extreme differences between substrate and coating, both in properties (316L high work hardening vs TiC purely elastic deformation) and chemical nature (316L metallic vs TiC covalent bonds). As such, it can be used to highlight general challenges pertaining to hybrid processes, and potential approaches/methods to deal with them.

The studied hybrid process involved two steps: an additive step, based on the deposition by DC magnetron sputtering of a pure titanium film (around 1 μm thick) on AISI 316L substrates followed by a transformation step, based on the conversion of the Ti film to TiC through low pressure gas carburizing.

The expected advantages of this approach include: a fast process (sputtering deposition being much faster for metals than for compounds [16]), better substrate/layer contact (initial metal on metal deposition), and flexibility (owing to the possibility of titanium partial conversion to keep a metallic interlayer). As a way to overcome its chemical complexity, this process can be viewed as two successive steps: first, the substrate/coating reactions happening as materials are heated before any carbon addition; and second, the high temperature interactions occurring between the new interfacial structures and diffusing carbon. This paper will deal specifically with substrate/titanium coating reactivity, during the first stages of a typical carburizing thermochemical treatment interrupted just before carbon introduction.

Understanding of the substrate/coating interfacial reactions and diffusion mechanisms is made arduous by chemical complexity (316L alloy containing Fe, Cr, Ni, Mo, Mn and C), and small layer thickness (leading to surface effects becoming non-negligible and restricting experimental analysis options). In order to overcome these difficulties, an iterative approach involving the successive study of increasingly complex model diffusion couples has been chosen:

- bulk Fe/Ti couple (simplified chemistry and geometry)
- bulk 316L/Ti couple (simplified geometry)
- sputtered Ti on 316L substrate (full chemical and geometrical complexity)

2. Materials properties

Describing every known interaction between titanium and 316L constitutive elements is outside the scope of this paper. Nevertheless, the work will be focused on the diffusion and solubility characteristics of the various experimentally identified phases. Due to the short dwell time of carburizing treatments, thermodynamic equilibrium is unlikely to be reached, and transitory states have also to be considered. In order to take into account these two complementary aspects in the interpretation of experimental results, elements solubility data from literature has been summarized in Supplementary Table 1 (a high solubility range being related to stabilizing effect of the concerned phase), while Supplementary Tables 2–4 present diffusion kinetics information at 1013, 1123, and 1223 K, respectively.

2.1. Iron

Iron presents thee allotropes: bcc α-Fe (alpha ferrite) stable up to 1185 K, fcc γ-Fe (austenite) stable between 1185 and 1667 K, and bcc δ-Fe (delta ferrite) stable over 1667 K. γ-stabilizing elements can be divided into isomorphous (Ni, Mn) and interstitials (C, N). Cr, Mo, Ti and Si are significant α-stabilizers present in this study. Oxygen shows an extremely low solubility (<0.1 at. % [17]), and its strong chemical affinity to iron promotes oxides precipitation over solid solution formation.

Elemental diffusivities from previous experimental data can be qualitatively arranged, showing considerable variations between allotropes:

$$D_C > D_O \gg D_{Ti} \simeq D_{Mo} \simeq D_{Mn} > D_{Ni} \simeq D_{Fe} > D_{Cr} \text{ in } \alpha\text{-Fe}$$

$$D_C > D_O \gg D_{Mo} > D_{Fe} \simeq D_{Cr} > D_{Mn} \simeq D_{Ni} > D_{Ti} \text{ in } \gamma\text{-Fe}$$

2.2. Titanium

Titanium exists as two main stable allotropes, an hcp α-Ti structure under 1155 K, and a bcc β-Ti structure at higher temperatures [18]. α-stabilizing elements are mostly interstitials (O, N, C), aluminium being the notable exception. β-stabilizers can be divided in β-isomorphous elements (Mo, Nb, V, Ta) and eutectoid elements (Mn, Cr, Ni, Fe, Si, Co, Cu).

Diffusion in α-Ti is known for its anisotropy, with single crystal diffusivities being 1.5 to 2.5 times higher in the basal plane than along the principal axis for Fe, Cr, Ni, and Mn [19]. Qualitative classification of diffusivities in polycrystals can be summarized from Supplementary Tables 2–4, independently from temperature, as follows:

$$D_C > D_{Fe} \simeq D_{Ni} > D_{Mn} > D_{Cr} > D_O > D_{Ti} \text{ in } \alpha\text{-Ti}$$

and $D_C > D_{Ni} > D_{Fe} \simeq D_{Mn} > D_{Cr} \simeq D_O > D_{Ti} > D_{Mo}$ in β-Ti

Main titanium allotropes show unusually low oxygen diffusivities at all temperatures compared to other interstitial elements. Together with the well documented solubility and reactivity of Ti phases with atmospheric dioxygen [20], this property makes oxygen contamination an easily overlooked potential diffusion parameter. While Nakajima et al. mentioned only moderate diffusivities decreases for Fe, Ni and Mn with small O additions (2.5 at. %) in α-titanium, effects of higher contents remain unknown [21].

Iron shows fast diffusion in pure titanium, especially in the α-allotrope. However, Peart et al. demonstrated that this behavior is highly sensitive to Fe contents at least in β-Ti, with 15 at. % addition leading to a four orders of magnitude diffusivity decrease [22].

2.3. 316L

316L is a low carbon quasi-austenitic stainless steel with only traces of ferrite (from Schaeffler diagram [23]). This fcc crystalline structure is stabilized by large nickel additions despite a high chromium content. Its combination of high corrosion resistance [24], work hardening [25–27] and ultimate tensile strain (50% at 650 MPa [28]) make it an alloy commonly used for mechanical applications in difficult media (such as chloride rich environments [29]).

2.4. Intermetallics

2.4.1. FeTi

FeTi intermetallic shows a CsCl bcc structure, with lattice constants close to those of α-Fe (+4% according to Ref. [30]). FeTi is known to be hard (measured elastic modulus up to 310 GPa [31]), abrasive resistant and brittle [32]. A large fraction of studies concerning this compound

are linked to liquid processes involving titanium and iron alloys (soldering, laser deposition, etc.), and concentrate on avoiding its formation to limit embrittlement [33]. Hydrogen storage has long been considered as a potential application [32,34], with research focusing on solid/gas interactions mechanisms and their consequences on crystalline structures [35].

Non-stoichiometry in this intermetallic is common, typically through iron deficiency. Element substitutions into the crystal lattice (partial or complete depending on the element) are likewise possible, with Cr, Ni and Mn replacing Fe, and Mo replacing Ti. In both cases, Suzuki et al. evidenced improved mechanical properties (higher hardness and yield stress) and a significant diffusion rate increase [36]. Substitution of iron by chromium up to 6 at. % [37] is accompanied by a shift towards titanium deficient non-stoichiometries. A possible replacement of iron by manganese up to 27 at. % was also mentioned [38]. Nickel has been shown [39] to fully substitute iron between 1176 and 1273 K, with no information available outside this temperature range. According to Knowles et al., molybdenum is only slightly soluble in FeTi, replacing titanium up to 2 at. % at 1173 K [40].

The only available diffusivity data for FeTi concerns titanium at 1223 K [41]. This element demonstrates a notably high self-diffusivity in the intermetallic compound, at least one order of magnitude higher than self-diffusion in pure titanium allotropes (see Supplementary Tables 2–4).

2.4.2. Fe_2Ti

Fe_2Ti is a Laves type C14 hexagonal phase. While limited literature was found in the past, this intermetallic compound has recently seen renewed interest due to the development of additive elaboration methods, such as laser melting [42], and improvements in welding processes [43], were it constitutes an undesirable byproduct. It is known to be hard (1242 HV0.5 [44]), and brittle [45].

As with all Laves phases, non-stoichiometry is common, chemical composition can be highly variable, and both iron and titanium can be substituted by other elements. Chromium was found to fully substitute iron over 823 K (no data available for lower temperatures) [37,46]. Phase changes to Laves C15 and C36 structures can occur at very high chromium contents (less than 8.5 at. % residual Fe for C36 and less than 2 at. % Fe for C15). Possible non-stoichiometric range of Fe_2Ti compound is diminished by Cr addition. Manganese likewise fully substitutes iron at 1273 K [38,47]. Nickel can partially substitute iron (up to 20 at. %), at least in the 1173–1273 K temperature range [39]. Molybdenum can fully substitute titanium between 1023 and 1173 K [40].

C14 Laves structure is sometimes referred in literature as lambda phase when either iron or titanium is replaced by other elements. Due to the lack of systematic investigations concerning Fe_2Ti and its variants, available information about phase stability covers only a limited temperatures range, and is especially lacking for room temperature. Furthermore, no recorded experiments have explored its self- or hetero-diffusion properties up to now.

3. Experimental methods

3.1. Bulk diffusion couples preparation

In order to compare their evolution under strictly identical conditions, Fe/Ti and 316L/Ti diffusion couples were associated in a single experimental setup called a diffusion triplet. It was composed of a four metal plates stack following the 316L/Fe/Ti/316L sequence (Fig. 1). This structure allows the study of three interfaces (316L/Fe, Fe/Ti, 316L/Ti) at the same time. Preparation methods applied to each plate in the stack are detailed below.

Square titanium plates of 10 × 10 × 3 mm (extracted from 406,4 × 127 x 6,35 mm sputtering targets), containing 9.5 at. % oxygen in solid solution (remaining from the powder metallurgy elaboration process) and less than 35 ppm of other elements (see Table 1), have been used as

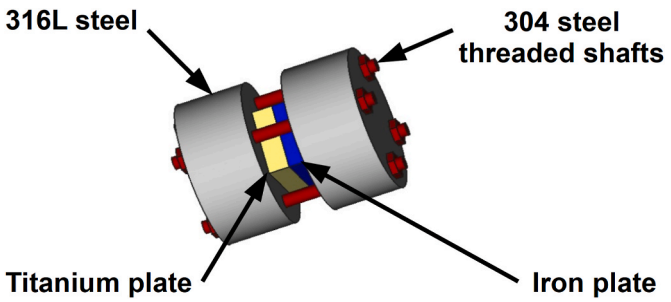

Fig. 1. Diffusion couples experimental setup.

the diffusion triplet first inner material. This Ti–O alloy composition evolves to a duplex α-β structure around 1223–1233 K [48]. Contact surfaces were mirror polished using an optimized sequence for pure titanium: SiC paper wet grinding up to P1200, followed by 9 and 3 µm diamond suspensions, and finally a mix of colloidal silica and H_2O_2 on cloth. Typical grain size was around 200 µm.

High purity 10 × 10 × 3 mm iron plates (extracted from 3 × 100 mm diameter sputtering targets) were used as the second inner material for the triplet. Metallographic examination revealed a classical polygonal and equiaxed microstructure, with grains (as revealed by 1% Nital etching) measuring around 65 µm. Small spherical inclusions (less than 5 µm diameter) were identified as FeO residues from the casting production process (see Supplementary Fig. 1-a,b). Contact surfaces were mirror polished using the following preparation method: SiC paper wet grinding up to P1200, followed by 3, 1, and ¼ µm diamond suspensions. Roughness parameters of 15 and 20 nm for Ra and Rq, respectively, were measured by optical profilometry.

Titanium and iron samples were placed between 10 mm thick 316L stainless steel plates (20 mm diameter) after ethanol ultrasonic cleaning. Their inner sides (in contact with titanium and iron, respectively) were mirror polished using a specified sequence: SiC paper wet grinding up to P1200, 3 and 1 µm diamond suspensions, followed by diluted colloidal silica on cloth. Optical profilometry measured roughness parameters of 15 and 20 nm for Ra and Rq respectively. Aqua regia etching revealed that grain size was in the 30 µm range (see Supplementary Fig. 1-c,d). Four 304 stainless steel threaded shafts ensured the continuous contact of the interfaces during the whole thermal cycle, thanks to 304 lower thermal expansion.

3.2. Sputtered diffusion couples preparation

In parallel to the bulk diffusion couples study, square laminated 316L square plates of 10 × 10 × 3 mm were used as substrates for PVD deposition. Initial microstructure (revealed by aqua regia etching) consisted of 20 µm equiaxed grains (see Supplementary Fig. 1-c). Deposition surfaces were prepared by mirror polishing (SiC paper wet grinding up to P1200, 3 and 1 µm diamond suspensions, and diluted colloidal silica on cloth), followed by 5 min acetone ultrasonic cleaning and ethanol final rinsing. Optical profilometry revealed roughness parameters of 15 and 20 nm for Ra and Rq, respectively.

Titanium was deposited in an industrial DC magnetron sputtering system (Kenosistec model KS40V–113K12). It should be noted that preliminary plasma cleaning is mandatory to obtain a durable contact between substrate and coating, leading to delamination during thermal treatment if disregarded. Detailed experimental conditions are summarized in Table 2.

Coating thickness after a 20 min deposition time was verified by optical profilometry and was equal to 1.3 µm. As expected with this deposition technique, roughness measurements showed values identical to the uncoated substrates. High oxygen presence in the deposited layers (24.5 at. %) was identified by EDS microanalysis, and is linked to similarly high contamination of the sputtering target. According to the

Table 1
Bulk plates compositions (ppm; B indicates balance).

	Ti	O	Al	Ca	Cr	Cu	Fe	Ni	Si	Mn	Mo	Co	V	Zr
Titanium	B	95,000	2.1	1.1	1.8	13	4.1	0.01	1	–	–	–	7.1	0.39
Iron	–	50,000	65	–	<10	66	B	42	34	48	<10	15	–	–
316L	–	–	–	–	191,600	–	B	113,000	14,800	20,100	14,400	–	–	–

Table 2
Experimental PVD coating conditions.

Titanium target			
Composition (at. %)	Ti = 75.5, O = 24.5	*Dimensions (mm)*	406 × 127 x 6
Plasma settings			
Power (W)	1500	*Voltage (V)*	−340
Current (A)	4.41	*Mode*	Direct current (DC)
Atmosphere	Argon	*Working pressure (mbar)*	4.4×10^{-3}
Argon flow (sccm)	80	*Residual pressure (mbar)*	7×10^{-6}
Motion settings			
Substrate movement type	Circular arc in front of target	*Arc radius (mm)*	95
Arc angle (°)	30	*Nominal speed (rpm)*	0.7
Duration (min)	20	*Total scans (passes in front of target)*	142

phase diagrams, titanium structure at this composition remains hexagonal (α) up to the melting point [48].

3.3. Diffusion conditions

Three thermal cycles (Fig. 2) differing only by their maximum dwell temperatures (1013, 1123 and 1223 K) were applied to three bulk diffusion triplets and three sputtered diffusion couples under secondary vacuum (5×10^{-5} mbar). The heating ramp was fixed at 9 K min^{-1} and the cooling was natural. Each dwell time had a duration of 15 min. These cycles correspond to typical low-pressure carburizing treatments (including degassing and plasma cleaning steps), shortened and optimized for shallow (1 μm) carbon diffusion. Observations were carried out after cross-sectioning, hot mounting and metallographic preparation. The procedure is identical to the one used for pure titanium, this protocol allowing simultaneous mirror polish for all phases initially present or formed in the diffusion triplets and couples.

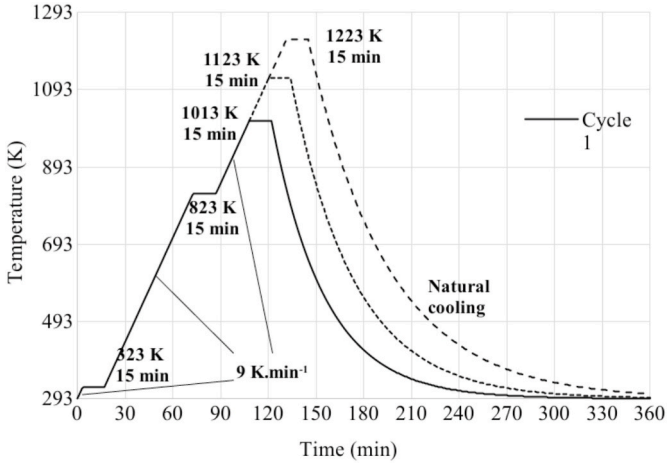

Fig. 2. Thermal cycles applied to diffusion couples.

3.4. Characterization methods

The analyses of the diffusion phenomena through interfaces were carried out at different scales. Macroscopic interfacial cohesion was assessed by optical microscopy (Olympus BX51 M coupled with Analysis software). Microstructural and morphological characterizations of the interfaces and surrounding materials were performed by scanning electron microscopy (JEOL 7610 F SEM-FEG) in secondary and backscattered electrons imaging. Qualitative chemical composition analysis of the phases was performed by energy dispersive X-ray spectrometry (EDS) profiles and mappings. Samples surface contamination was removed by a 5 min plasma etching in the microscope airlock before each measurement. Investigated elements were Fe, Ti and O for Fe/Ti interfaces, with the addition of Mo, Mn, Ni, Cr, and C for 316L/Ti interfaces. For light elements (C, O) analyses were carried out at 5 kV acceleration voltage, while 15 kV were used for other elements. Elemental analyses were limited by two main factors. First, the uncertainty of the EDS technique was estimated around 1 at. % for almost all elements. Titanium is a significant exception, as its Lα line is difficult to decorrelate from EDS spectra background noise. Consequently, low titanium contents (0–1 at. %) are typically overestimated (+5 to 7 at. %) in samples analyzed at 5 kV acceleration voltage, while values obtained at 15 kV (using Ti Kα line) are reliable. Secondly, the relatively low lateral resolution of the EDS technique under standard conditions (1 μm) did not allow a discrete analysis of sub-micron structures formed at the interfaces. Fine elemental analyses of the Ti/316L diffusion couple thermal treated at 1223 K (EDS mappings and profiles) were obtained by transmission electron microscopy (TEM). They were performed on a thin foil (8 × 5 × 1 μm thickness) centered on the Ti/316L interface prepared by focused ion beam (FIB) milling using a ThermoFisher Helios NanoLab600i apparatus (see Supplementary Fig. 2). An accelerated ion beam with a 2 kV voltage was used for 10 min to finish the FIB lamella milling. These analyses aimed primarily at correlating microstructures visible in SEM with metallurgical phases, for identification purposes in the other samples. As such, they were only performed for the bulk Ti/316L couple at the highest temperature (Cycle 3 in Fig. 2), where structural and phases variety were maximum. STEM-EDS was performed on a Philips CM20 FEG HF3300 microscope operated at 200 kV equipped with a Brüker SDD detector.

4. Results and discussion

Experimental results will be presented by decreasing length scale, progressively focusing on the diffusion couples interfaces: the integrity of diffusion couples (10 mm), the microstructural modifications of the materials forming the couples (10 μm), and finally the direct alterations happening around and inside the interfaces (1 μm). At each scale, systematic comparison between configurations of increasingly complex chemistry and geometry (bulk Ti/Fe, bulk Ti/316L and sputtered Ti/316L) have been carried out to clarify the underlying chemical reactivity and diffusion mechanisms.

4.1. Diffusion couples integrity

Macroscopic observations concerning the junction of diffusion couples interfaces with temperature are detailed in Table 3. They revealed a major effect of titanium presence.

Every couple involving titanium (whether sputtered or bulk) showed

Table 3
junction formation in diffusion couples depending on dwelling temperature.

	Bulk 316L/Fe	Bulk Ti/Fe	Bulk Ti/316L	Sputtered Ti/316L
1013 K	No junction	Full junction	Full junction	Full junction
1123 K	No junction	Full junction	Full junction	Full junction
1223 K	50% contact surface joined	Full junction	Full junction	Full junction

a complete contact between materials starting from 1013 K. On the other hand, Fe/316L junction did not form, and no mechanical strength could be observed until 1223 K. The junction was only partial at this temperature, with more than 50% of the interface consisting of porosity as revealed by optical microscopy observations. This difference can be attributed to two main reasons. First, the initial direct contact between iron and steel is delayed due to the passive oxide layer present between the two materials. In the case of the couples containing titanium, however, titanium strong affinity for oxygen [20] allows the low temperature destabilization of the oxides and the early junction formation. Secondly, Fe/316L interaction relies mostly on iron self-diffusion, which is at least two orders of magnitude slower (see Supplementary Tables 2–4) than titanium diffusion in iron, explaining the slow porosity elimination observed, even once direct metal/metal contact is established.

As bulk 316L/Fe diffusion couples could not be adequately joined under the experimental conditions described in 3.3, their diffusion properties will not be discussed further.

4.2. Long-range microstructure

The possibility of long-range diffusion is limited to bulk diffusion couples, as the sputtered layer shares the same spatial scale as the interfacial compounds formed during the experiments (micrometer range). To complete microstructural observations and EDS measurements, apparent diffusivities were estimated for each visible layer through dimensional analysis. Systematic comparison with diffusion data for elements in various phases (Supplementary Tables 2–4) can provide insight into the underlying formation mechanisms. Fig. 3 presents the SEM observation for bulk Fe/Ti and 316L/Ti diffusion couples at 1123 and 1223 K. After the thermal cycles at 1013 K, microstructural alterations are limited to the interface, while higher temperatures allow diffusion beyond the junction. The chemical reactivity remains local, up to a temperature ranging between 1013 and 1123 K, at which stage elements can begin to diffuse through the interface. As noticeable when comparing Fig. 3-a/3-c and Fig. 3-b/3-d, microstructural elements for each given temperature are essentially the same, independently from the presence of 316L or iron in the diffusion couple.

At 1123 K, two successive layers are present on the titanium side, while no large-scale structure variation is visible on the iron/steel side. Closest to the interface, a 5 μm thick homogeneous layer can be identified as β-Ti. EDS measurements revealed a stable composition containing around 12 at. % iron in titanium, with no significant oxygen presence. Dimensional analysis, taking into account the distance from the interface, allows to associate a diffusivity of $D_1 = 2.8 \times 10^{-10}$ cm^2 s^{-1} to this layer. This value matches the *oxygen diffusivity in titanium* (instead of the expected iron diffusivity in titanium) at this temperature (as seen in Supplementary Tables 2–4). A 10 μm thick second layer shows a α/β-Ti duplex structure, with crisscrossed needles/platelets contained in a matrix visually similar to the first layer. These needles are submicrometric, and their density hints at a percolating network layout. Local elemental analyses, due to this high structural refinement, cannot give direct access to phases compositions, but global EDS measurements revealed lowered iron contents (9–10 at. % Fe) compared to the previous layer. Under the hypothesis of a matrix identical in composition to the first layer, needles can be deduced to contain a reduced amount of iron, hinting at oxygen rich residual α-Ti, which was confirmed by the anti-correlation between iron and oxygen concentrations measured in the duplex structure (Supplementary Fig. 3). Dimensional analysis, taking into consideration the distance from the interface, associates a diffusivity of $D_2 = 2.5 \times 10^{-9}$ cm^2 s^{-1} to this layer, corresponding to iron

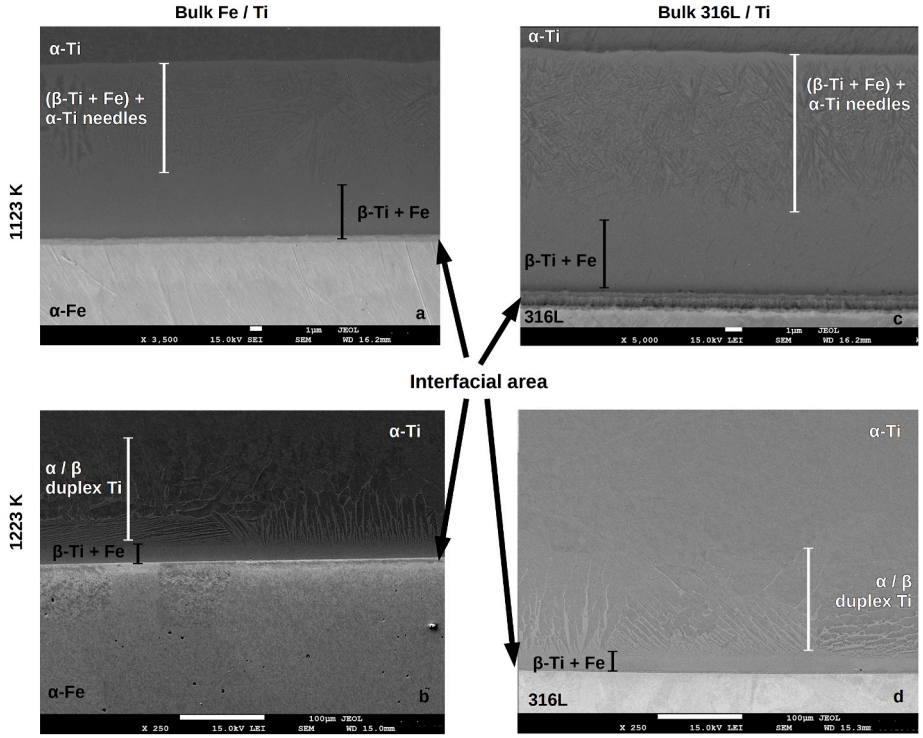

Fig. 3. Long-range microstructures for bulk Fe/Ti and 316L/Ti diffusion couples at 1123 and 1223 K (SEM imaging).

diffusivity in β-titanium at 1123 K (Supplementary Tables 2–4). The lack of microstructure modification in iron/steel can be ascribed to the much lower (around two orders of magnitude) diffusivity of titanium in austenite and ferrite.

These elements allow to draw the three following inferences concerning long-range diffusion at 1123 K:

- As revealed by EDS analyses, iron, and to a lesser extend nickel, are the only elements of 316L steel to effectively diffuse through the interface. This effect cannot be related to diffusivity differences between Fe and other elements (Supplementary Tables 2–4), as successive diffusion fronts corresponding to each species are not observable. *Thus, interfacial structures act as a filter or trap for most stainless steel elements.*
- The existence of two long-range microstructures can be explained by the insolubility of Fe (O respectively) in α-Ti (β-Ti respectively). α to β transformation in titanium is triggered by the contact with iron, rejecting oxygen from it. As diffusivity of oxygen in α-Ti is ten times lower than that of iron in β-Ti (Supplementary Table 2), oxygen remains trapped behind the iron diffusion front, stabilizing residual α-Ti inclusions. Observed needle/platelet shape can be linked to diffusion anisotropy in hexagonal α-Ti [49,50]. Needles percolation constitutes pathways that allows progressive diffusion of oxygen towards the untransformed titanium before the iron diffusion front. This slow oxygen elimination mechanism explains the formation and growth of the first layer from the second one. As a summary, the first layer corresponds to fully transformed iron-rich β-Ti, whose advance is controlled by oxygen rejection, while the second layer corresponds to the macroscopic α to β titanium transformation, controlled by iron diffusion.
- Long-range structures formation is controlled by iron and oxygen diffusion titanium. Effects of titanium α to β transformation kinetics and iron diffusion through the interface are negligible in the detailed experimental conditions.

Structures observed at 1223 K are globally similar to their lower temperature counterparts, with the same double homogeneous/duplex aspect, and lead to the same conclusions. The layer closest to the interface consists of 15 μm thick β-titanium. EDS microanalyses showed exactly the same composition as the analogous structure at 1123 K (12 at. % iron in titanium, no significant oxygen amount). Dimensional analysis (using the distance from the interface), gives a diffusivity of $D_3 = 2.5 \times 10^{-9}\ cm^2\ s^{-1}$, confirming that oxygen diffusion in β-titanium is the controlling mechanism for this layer growth (Supplementary Tables 2–4). The second (duplex) layer shows a gradient structure very similar to the one observed during titanium/stainless steel diffusion bonding by Poddar [51]. It evolves from β-titanium (12 at. % iron in titanium) platelets in α-titanium matrix on the iron (or steel) side, to a percolating β-titanium network in intergranular position between α-Ti grains. Due to the absence of a clearly defined delimitation with unaffected titanium, this region thickness can only be qualitatively estimated around 135 μm. While Poddar [51] interpreted this microstructure as the result of partial retention of high temperature β phase, this mechanism cannot be confirmed by the observations performed in the present study. Stabilizing effect of measured oxygen contents (9.5 at. %) is sufficient to ensure that titanium remains as α allotrope in the whole temperatures range (up to 1223 K). As a consequence, β-Ti can only be formed under direct influence of diffusing iron. The structural gradient can be interpreted as the result of iron fast grain boundary diffusion, associated with local α to β transition, followed by bulk lateral diffusion inside grains along preferential crystallographic directions, thus leading to the platelet shape of residual α-titanium. Similarly to 1123 K, long range microstructure in iron/steel is visibly unmodified. Low diffusivity of titanium in austenite and ferrite can explain this observation. The comparison between the results obtained for the samples exposed at 1123 K and 1223 K suggests that iron diffusion increases faster with temperature at titanium grain boundaries than in single crystals. These results contradict former studies (see Ref. [52] for general considerations on grain boundary vs lattice diffusion, and [53] for the case of α-titanium self-diffusion in particular), which evidenced a general trend of convergence between diffusion modes at higher temperatures in various metals. Two main interpretations could explain this discrepancy. A yet unspecified, anomalous diffusion behavior at grain boundary for the iron/titanium couple. In the absence of experimental proof, this possibility is supported by several irregularities reported when these elements interact. Examples include vacancies stabilization by iron additions in titanium [53], or iron complexes formation at grain boundaries [54]. A more complex grain boundary diffusion mechanism, that could be based on iron and oxygen incompatibility in titanium (each being soluble in and stabilizing a different allotrope), and leading to a lower apparent grain boundary diffusion rate. Since significant iron diffusion can only happen in β-titanium, oxygen (either as a deliberate alloying component or an elaboration process contaminant) has to be depleted first, in order to allow the α to β transition. As a consequence, initial concentration and lateral rejection rate of oxygen to the neighboring α-titanium grains control the phase transformation advancement. At low temperatures (≤1123 K), this inhibiting effect is sufficient to reduce iron apparent grain boundary diffusion to similar levels as bulk diffusion, leading to the observed flat α/β titanium macroscopic interface. At higher temperatures (1223 K), oxygen diffusion in α-titanium is thermally activated. Lateral rejection of oxygen is quick enough to allow unhindered advance of iron in titanium grain boundaries. α to β titanium transition occurs first at boundaries, followed by a slower progression in grains along preferential crystalline directions.

4.3. Interfacial microstructure

Small scale microstructures (Figs. 4–6) developed at the interface and the corresponding composition profiles show considerable variation depending on the considered materials. Consequently, experimental results will be provided separately for each diffusion couple, in order to better highlight their evolutions with temperature.

4.3.1. Bulk Fe/Ti

At 1013 K, a heterogeneous (with dark spots) 250 nm layer is present at the iron/titanium interface (Fig. 4-a). Due to its low thickness, exact composition cannot be determined by SEM-EDS microanalysis. Classical Fe/Ti binary diagram [55] supports its identification as intermetallics (FeTi and/or Fe_2Ti). Observed dark spots can be interpreted as either pores (consequence of an incomplete contact between plates at this temperature), or the result of mixing between FeTi and Fe_2Ti compounds. Small scale diffusion of iron is evidenced by the transformed 750 nm β-Ti layer visible on the titanium side.

At higher temperature, the structures change, then remain qualitatively the same at 1123 and 1223 K They consist of two consecutive layers of the same thickness (175 nm for 1123 K in Fig. 4-b and 350 nm for 1223 K in Fig. 4-c) at the interface. Composition evaluation by EDS analysis suggests the formation of the intermetallic compounds FeTi (on titanium side) and Fe_2Ti. Despite highly favorable conditions (Fe diffusivity in Ti around 100 times higher than the reverse), neither porosity nor microstructural alteration could evidence any measurable Kirkendall effect.

Literature addressing pure iron/titanium interdiffusion is both limited and inconsistent regarding intermetallics formation: none [56], only FeTi [41], only Fe_2Ti [57], and both [58]. It is noteworthy that Kirkendall effect is only reported when no intermetallics are formed [56], establishing an incompatibility with intermetallics presence. Considering unit cell expansion during titanium to intermetallic transformations (+125% volume/Fe atom for FeTi, and +72% volume/Fe atom for Fe_2Ti, according to lattice constants data [59]), *these phase changes can be understood to trap defects and act as sinks for Kirkendall vacancies*. Consequently, *Fe/Ti intermetallics seem to preclude voids*

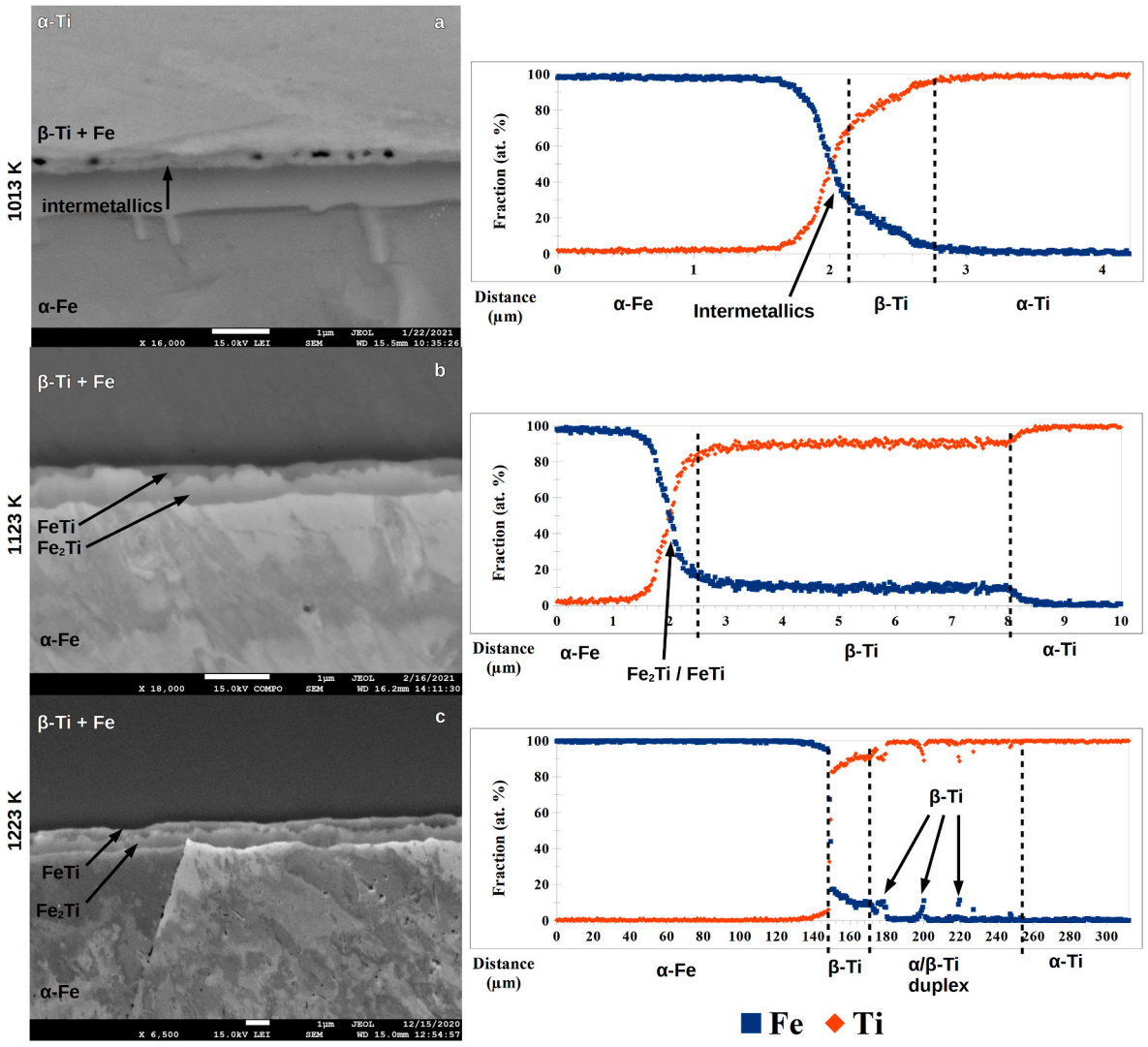

Fig. 4. Interfacial microstructures evolution for bulk Fe/Ti (SEM imaging), and corresponding EDS composition profiles.

nucleation near the interface. From the literature results, intermetallics formation itself seems dependent on experimental conditions, and can probably be traced back to initial interface properties (macroscopic geometry, roughness, oxidation, grain sizes, impurities segregation, etc.).

No significant titanium diffusion (>1 µm) is measurable in iron, which is consistent with literature diffusivity values provided in Supplementary Tables 2–4.

Intermetallics thickening (+100% between 1123 and 1223 K) is proportionally less than iron diffusion advancement in titanium (+800% between 1123 and 1223 K), suggesting that their *growth is thus controlled by compounds formation kinetics rather than Fe diffusion* under the considered experimental conditions.

Growth directions for each intermetallic compound are difficult to infer from experimental observations alone. Thermodynamic data from various sources summarized by Gasior et al. [60] consistently classified Fe_2Ti formation enthalpy lower than that of FeTi. Fe_2Ti to FeTi transformation is consequently disfavored, and *FeTi layer can only grow towards titanium*. Furthermore, the matching thicknesses of layers reveal that formation kinetics of FeTi and Fe_2Ti intermetallics are either equivalent if layers grow in opposite directions, or that FeTi formation is twice as fast as Fe_2Ti if both layers grow towards titanium.

4.3.2. Bulk 316L/Ti

The observed microstructures for this diffusion couple are more complex, and phases identification requires coupling SEM observations with EDS profiles (Fig. 5-a to -c).

At 1013 K, the backscattered electrons images (Fig. 5-a) reveal the formation of four different layers between 316L and titanium. The first two on titanium side (200 and 100 nm, respectively) correspond to consecutive diffusion fronts in titanium. EDS profile (Fig. 5-a) indicates iron enrichment in the first layer, and both nickel and iron in the second one. According to the diffusivity data in Supplementary Tables 2–4, iron and nickel diffusion in α-Ti are similar and faster than other 316L constitutive elements. Diffusion kinetics can thus not explain nickel delayed diffusion in α-Ti. Similarly to the mechanism presented for Fe/Ti diffusion couples, iron diffusion front (>12 at. % Fe) correlates with titanium α-to-β phase transformation. According to Fe/Ti [55] and Ni/Ti [61] binary diagrams, iron is a stronger β stabilizer than nickel. At 1013 K, allotropic transformation can only be triggered by Fe. Significant Ni solubility (see Supplementary Table 1) is limited to β-Ti allotrope, explaining the diffusion delay observed. This effect is probably compounded by the increased solubility of nickel in titanium with iron additions [62]. Iron total diffusion distance (300 nm) is smaller than the one observed for Fe/Ti couple (750 nm) under the same conditions (Fig. 4-a), suggesting a slight delay in 316L/Ti contact formation. This hypothesis is supported by larger local porosity visible in the interfacial

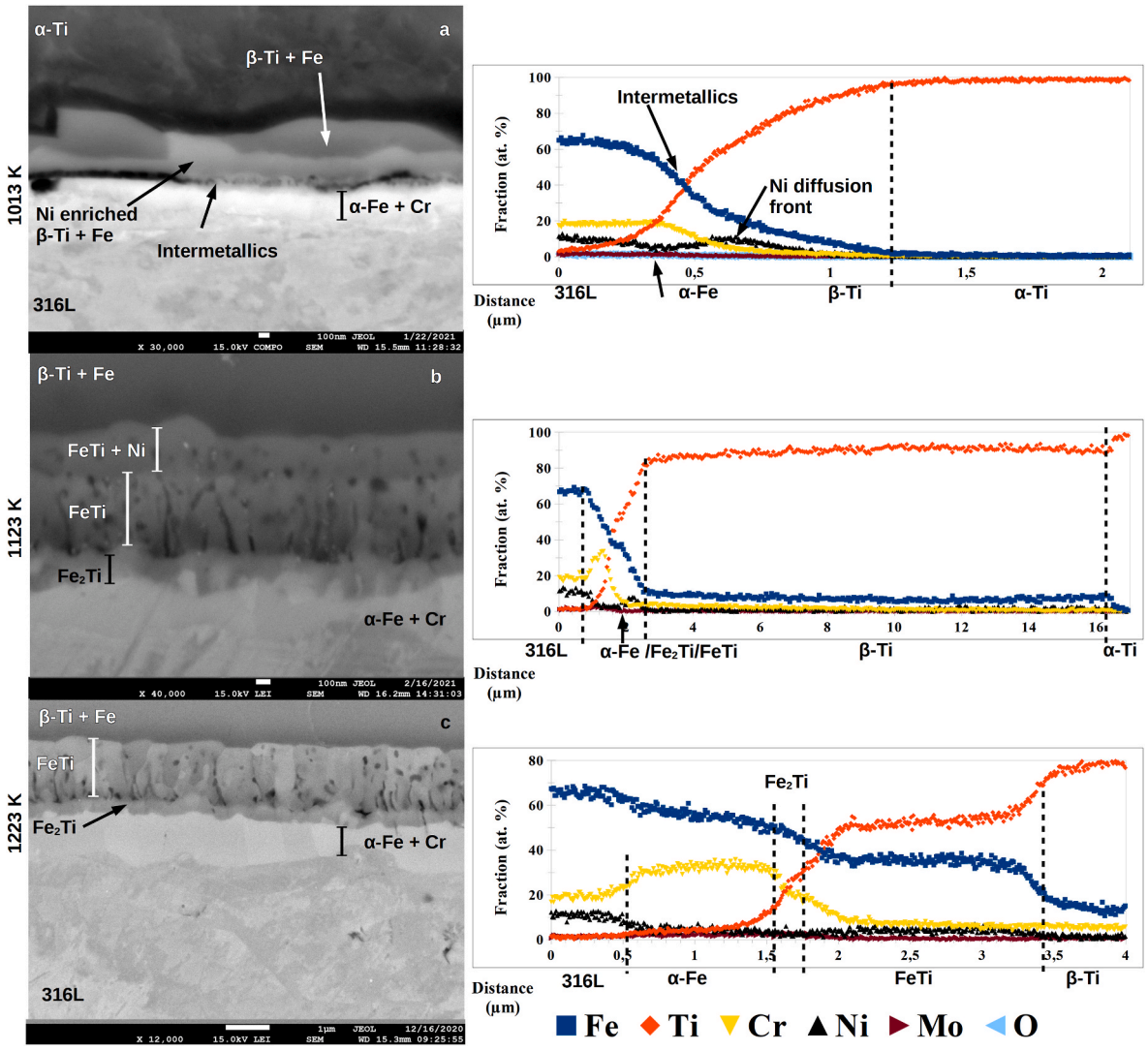

Fig. 5. Interfacial microstructures evolution for bulk 316L/Ti (SEM imaging), and corresponding EDS composition profiles - Note: image a was taken using back-scattered electrons imaging, to better highlight compositional variations near the interface.

layer (left of Fig. 5-a). *Delayed contact can be ascribed both to generally slower diffusion in austenite compared to ferrite, and higher stability of passive oxide on 316L than pure iron.* A final layer (150 nm thick) is present on 316L side. EDS profiles (Fig. 5-a) indicate a qualitative decrease in nickel and iron local concentrations, but its low thickness does not allow formal identification of this additional phase. However, austenitic steels and titanium interdiffusion has been studied in literature under longer dwell times, leading to thicker and easier to analyze interfacial layers: [51,63–68]. Most authors report a similar structure, and correlate the layer composition with ferrite, the only exception being Ghosh et al. [69], whose interpretation involved sigma phase (FeCr intermetallic) formation.

Interfacial layers grow both in size and complexity at 1123 K (Fig. 5-b). The first two layers on titanium side (250 nm and 550 nm respectively) share a similar aspect, with a network of fine dark spots and lines normal to the interface. EDS profiles (Fig. 5-b) reveal a very local increase of nickel concentration (>8 at. %) in the first layer, while the second one contains mostly titanium and iron in equal contents with small amounts of nickel (4 at. %). Considering that iron can be fully substituted by nickel in FeTi (Supplementary Table 1), it can be concluded that *these two layers correspond to a single,* 800 nm *thick, FeTi crystallographic phase,* with chemical composition variations related to successive growth steps. The comparison with the equivalent layer in Fe/Ti couple (Fig. 4-b) shows a slower growth, while long range diffusion of elements is essentially the same. These observations confirm FeTi evolution characteristics. FeTi grows by advancing in the β-Ti layer. *Intermetallic growth is controlled by compounds formation kinetics*. This mechanism explains activation energies divergences reported in literature for reaction layers [63]. Most authors incorrectly assumed that such growth is diffusion controlled. Growth depends on intermetallic composition. FeTi formation is four times faster when integrating elements from 316L stainless steel than for pure iron.

The third layer is identical in morphology and thickness (200 nm) to the corresponding one observed in Fe/Ti couples (Fig. 4-b), and can be identified as Fe_2Ti. The last layer on 316L side (500 nm) is associated to a marked increase in chromium contents, up to a concentration higher than that initially present in 316L steel (35 at. % against 19 at. %, respectively - Fig. 5-b). Local composition, qualitatively estimated by EDS measurements (35 at. % Cr, 5 at. % Ni, 5 at. % Ti, 55 at. % Fe), corresponds to the ferritic domain of the Schaeffler diagram [70]. Chromium segregation near the interface between titanium and austenitic steels was reported by many authors, and its origin variously interpreted. Kale et al. explained it as a residue from stainless steel passive oxide [66]. This hypothesis seems contradicted by two evidences: first of all, measured chromium concentration and layer thickness correspond to much higher Cr amounts than what is typically

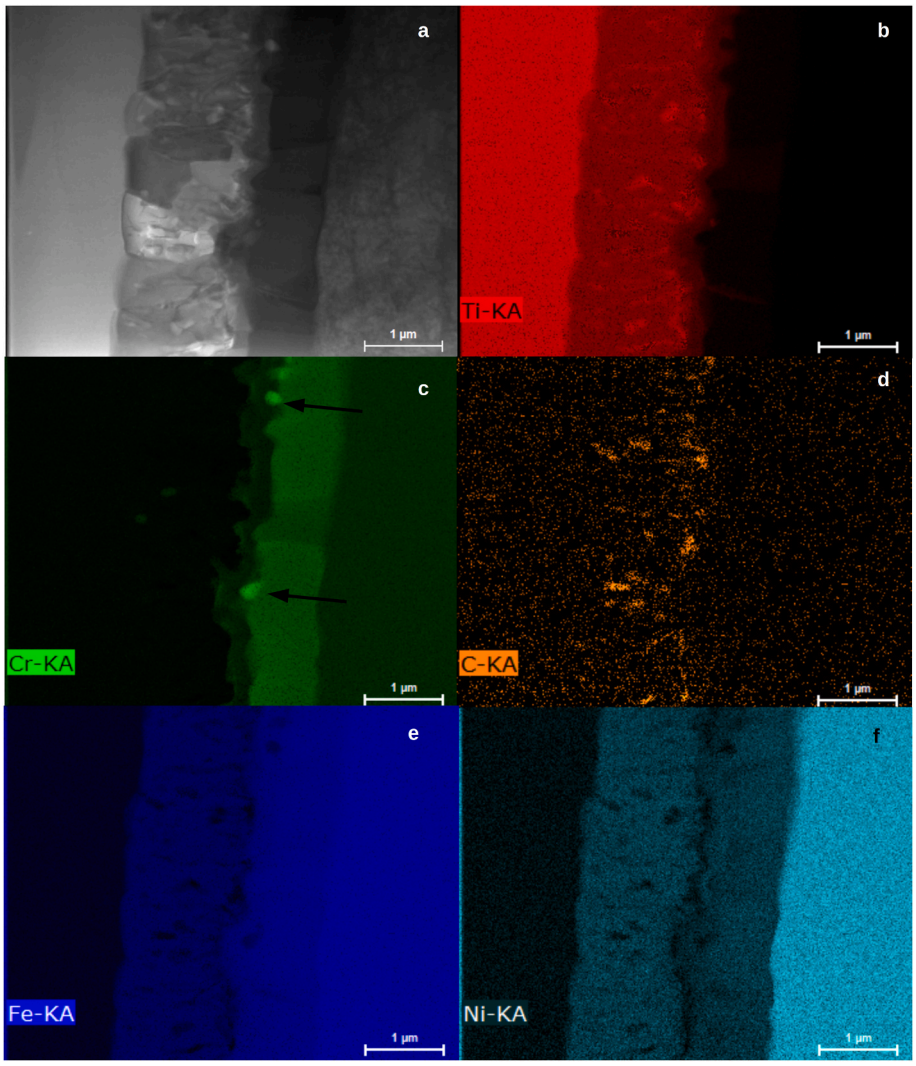

Fig. 6. Interfacial STEM-EDS elementary mappings for bulk 316L/Ti at1223 K. a – TEM bright field imaging; b – titanium mapping; c – chromium mapping, arrows indicate 150 nm chromium segregations; d – carbon mapping; d – iron mapping; d – nickel mapping.

available from a spontaneous oxide covering (<2 nm according to Wang et al. [71]); secondly, Cr segregation increases with temperature (as observed by comparison on Fig. 5-a and 5-b). Other authors interpretation focuses on the existence of a chromium chemical activity gradient, caused by titanium diffusion in steel [51,65,67]. This effect would be stronger than that of Cr concentration gradient, and lead to uphill diffusion towards the interface. However, the measured thickness of Cr enriched area (500 nm thick) corresponds neither to theoretical diffusion depth for Ti in α-Fe (2 µm using data from Supplementary Tables 2–4), nor that of Ti in γ-Fe (20 nm).

A simpler explanation can be formulated from the characterizations performed in the present study. Considering that EDS microanalysis is based on elements concentrations *relative* to each other, the measured increase in chromium contents could be linked to simple local depletion of the other elements instead of chromium segregation per se. As previously demonstrated, iron and nickel (main γ-stabilizing element) quickly move across the interface and diffuse into titanium; due to very low self-diffusivity in γ-Fe (Supplementary Tables 2–4), the replacement of depleted iron is slow, causing γ to α transformation near the interface. This mechanism is further magnified by increased iron self-diffusivity in ferrite, leading to an apparent chromium segregation. Ferrite layer growth depends on the balance between iron availability from 316L and its depletion due to diffusion towards titanium. This could explain the limited Fe depletion measured in ferrite compared to the amount of iron transferred to titanium. It can be noted that both titanium diffusivity and solubility are greatly increased in α-Fe compared to γ-Fe (Supplementary Tables 1–4). Under the iron/nickel depletion hypothesis, Ti diffusion in 316L can be understood as a consequence rather than the cause of austenite/ferrite transformation.

At 1223 K, the microstructures display no qualitative evolution compared to 1123 K. Interfacial layers (Fig. 5-c) show the same appearance, and SEM-EDS profiles (Fig. 5-c) are similar to those measured at 1123 K. However, STEM-EDS maps (Fig. 6) and profiles (Fig. 7) revealed additional details on formation mechanisms and phases evolution.

FeTi layer is much larger (1400 nm) than its equivalent in the Fe/Ti couple, confirming that the growth of this compound is not primarily diffusion controlled, and chemical composition dependent. The separation as two sublayers (corresponding to variable Ni contents) visible at 1123 K is not observable at 1223 K, and TEM-EDS profiles (Fig. 7) evidence a more homogeneous composition corresponding to $Fe_{0.8}Cr_{0.1}Ni_{0.1}Ti$. These observations show that nickel and chromium are integrated at higher temperatures, both in newly grown FeTi intermetallic and to already formed FeTi layer, leading to bulk compositional changes during thermal cycles. According to Gasior et al., partial iron substitution with nickel in FeTi stabilizes the intermetallic compound [60]. *Late integration of nickel and chromium can thus be interpreted as the transition between low temperature, formation kinetics, controlled growth*

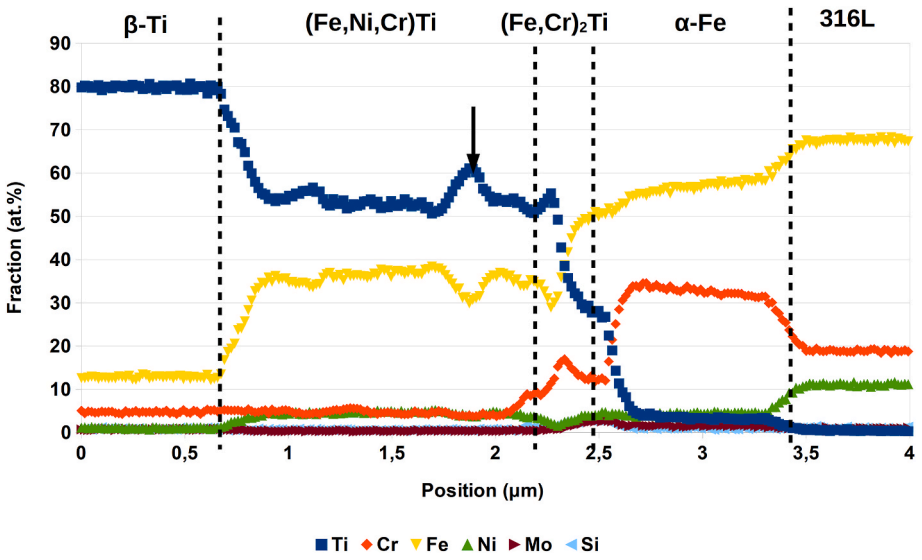

Fig. 7. STEM-EDS elementary profile across the interface for bulk 316L/Ti at 1223 K. Arrow: titanium carbide grain.

(FeTi) to a high temperature regime, linked to thermodynamic stability ((Fe,Cr,Ni)Ti). Attempts to formally identify the phase structure through TEM diffraction met no success, due to pattern superimposition along the thin foil thickness and to the limited accuracy of lattice distance measurements in the reciprocal space using electron diffraction. However, this observation, together with TEM bright field images (Fig. 8), evidence *submicron grain size (*100 nm*) in this layer*.

Fig. 5-c shows dark spots and lines normal to the interface. A similar structure was interpreted by Shirzadi et al. as pure titanium, without providing any formation mechanism [68]. However, STEM-EDS maps comparison revealed that these spots contain both titanium (Fig. 6-b) and carbon (Fig. 6-d), suggesting formation of TiC as the more likely candidate. Simple image analysis on SEM pictures reveals a volume fraction around 8% for TiC in FeTi layer. Such carbon concentration is beyond what is available from iron directly involved in FeTi crystallization: *titanium carbides grow after intermetallic formation*, under the effect of a carbon flux originating from stainless steel. This hypothesis is further supported by TiC particles alignment and morphology, which highlight carbon diffusion pathways through FeTi layer. Finally, TiC very low formation enthalpy (-184.10 kJ mol^{-1} [72]) confirms that the proposed mechanism is thermodynamically possible. In keeping with non-significant carbon contents measured in titanium, FeTi intermetallic acts as a filter, trapping this element in the layer. Titanium carbide formation is controlled by local carbon diffusion, which is confirmed by experiments performed by on titanium/high carbon steel diffusion couples, where carbon immediate and massive availability after materials junction led to interfacial formation of TiC instead of intermetallics [73].

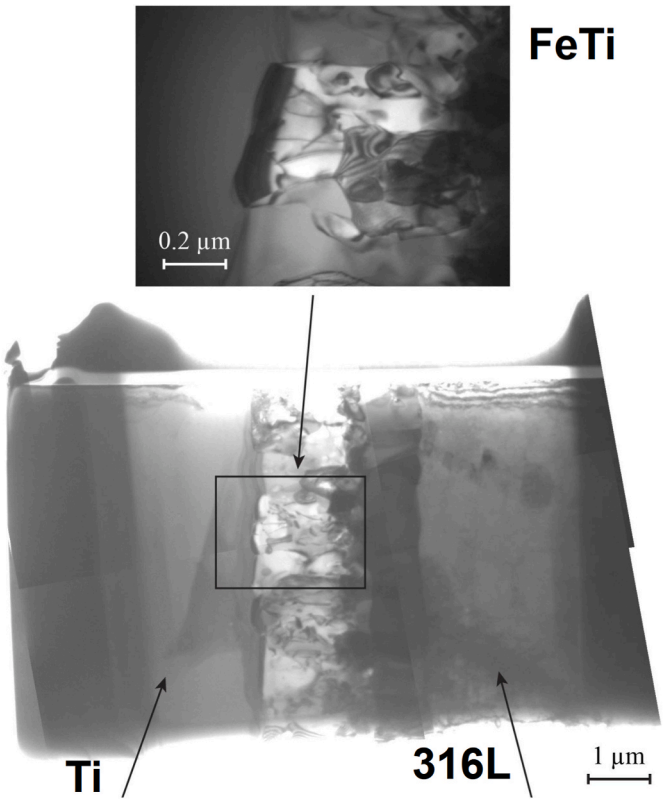

Fig. 8. TEM bright field imaging across the interface for bulk 316L/Ti at 1223 K (left: Ti, right: 316L).

As evidenced by STEM-EDS profile (Fig. 7), Fe_2Ti phase composition shows local chromium segregation (18 at. %) close to the solubility limit (Supplementary Table 1). At the same time, nickel contents decrease (<2 at. %); this can be attributed to either an incompatibility due to chromium substitution, or a stronger affinity with the neighboring FeTi phase. The layer is thinner (250 nm – Fig. 5-c) than its equivalent in the Fe/Ti diffusion couple (350 nm – Fig. 4-c), showing minimal increase between 1123 and 1223 K. Such growth inhibition can be ascribed to the chromium enrichment of neighboring ferrite layer: indeed, thermodynamic computations [74] show an increase of Fe_2Ti formation enthalpy when Fe is even moderately substituted by Cr, disfavoring intermetallic compound formation towards stainless steel. These observations also confirm that *Fe_2Ti phase grows through progression towards 316L*.

Transformed ferritic layer (950 nm) shows large grains around 800 nm. The resulting columnar structure, normal to the interface (Fig. 5-c and Fig. 6-a), suggests a slow crystallization from 316L. Long-range progression of iron in titanium and ferrite growth between 1123 and 1223 K are largely uncorrelated, which confirms that *α-Fe is not the only source for iron diffusion in titanium*. STEM-EDS profiles (Fig. 6) evidence the uphill chromium gradient (31–35 at. %) formerly reported by several authors [67,68], and a similar but opposite iron gradient. Titanium contents are stable along the ferritic layer thickness (4 at. %), further confirming that Cr segregation is caused by Fe depletion rather than Ti penetration in 316L steel. Layer evolution thus depends mainly on a dynamic balance of iron diffusion. Small chromium-rich grains

(<100 nm) are visible at the interface between Fe_2Ti and ferrite (Figure -6c, indicated by arrows). Considering errors due to grain/matrix superimposition, typical compositions (50 at. % Cr, 35 at. % Fe, 10 at. % Ti) identify these particles as sigma phase FeCr [37,75]. Nucleation of this new phase is probably triggered by a local increase of the iron depletion, as titanium additions are instead known to inhibit FeCr intermetallic compound formation (Fe–Cr–Ti phase diagram [46]). This mechanism is supported by former works [71,74]: longer dwelling times lead to continuous sigma phase layer at the interface between Fe_2Ti and ferrite, as well as its progression along ferrite grain boundaries towards steel. Sigma phase grains formed in contact with Fe_2Ti may also have a pinning effect on the ferrite/Fe_2Ti boundary, further inhibiting the neighboring intermetallic compound growth.

4.3.3. Sputtered Ti/316L

As mentioned in part 3.4, two different settings have been used for SEM-EDS analysis. Due to the interactions identified between oxygen and other solute in titanium for bulk diffusion couples (part 4.2), composition profiles presented in Fig. 9-a to -c were obtained in experimental conditions optimized for light elements (SEM 5 kV acceleration voltage). Improved lateral resolution is a well known secondary benefit of lowered acceleration voltages during EDS measurements, reducing the analyzed region to 100 nm diameter [76]. As already mentioned in experimental methods description, titanium concentration in 316L is overestimated under these conditions. Quantitative analysis of 316L constitutive elements is not visible on profiles a to c of Fig. 9, but was nonetheless carried out, and will be described in the following paragraphs. Secondary electrons SEM images (Fig. 9-a, 9-b, 9-c) appear substantially different from bulk samples, despite the presence of similar phases, which can be attributed to edge effects during samples preparation (micrometer scale coating), and low SEM acceleration voltage (highlighting surface topology).

In samples treated at 1013 K, the layered structure obtained around the interface (Fig. 9-a) is identical in both compositions and sizes to the one formed during bulk Ti/316L diffusion. Starting from titanium side, it can be described first as non-transformed α-Ti (around 1100 nm thick), with oxygen contents around 25 at. % (Fig. 9-a). This phase is mostly unaffected by diffusion phenomena, and retains the properties of the initial titanium coating. A second 100 nm thick layer of titanium contains 12 at. % iron, highlighting Fe diffusion and subsequent α-to-β titanium phase transformation. Thickness is similar, if a bit smaller, than the equivalent layer in bulk diffusion couples (200 nm), and could be ascribed to non-significant local diffusion variations or diffusion delays. A second diffusion front corresponds to nickel enrichment of transformed β-Ti (100 nm). The next structure is a very thin darker layer (<100 nm), that can be interpreted as intermetallics starting to form at the initial interface between titanium and stainless steel. The final area is located inside 316L (150 nm), and composed of iron and nickel

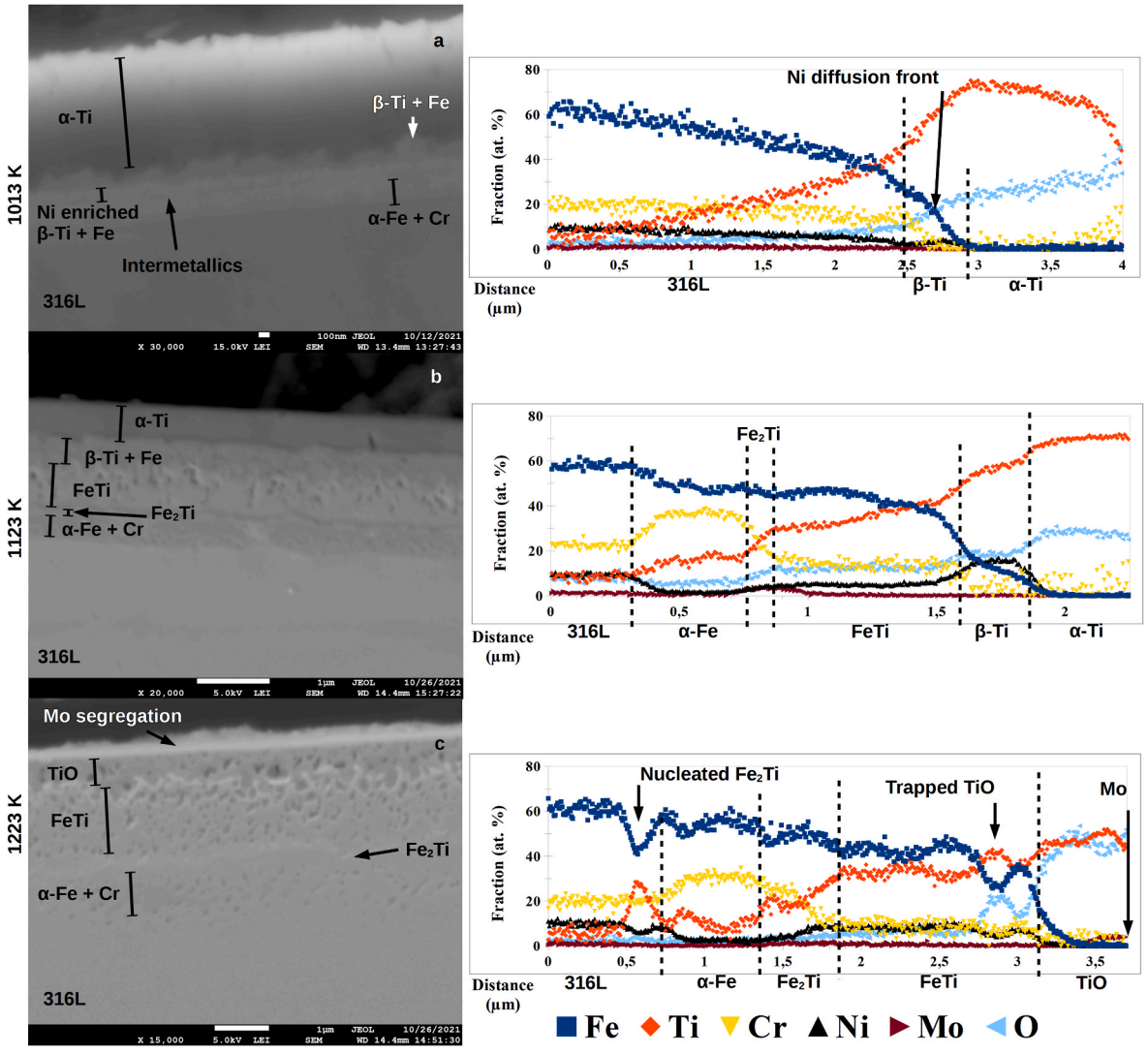

Fig. 9. Interfacial microstructures evolution for sputtered Ti/316L (SEM imaging), and corresponding EDS composition profiles.

depleted ferrite.

As a conclusion, *substitution of bulk titanium by PVD coatings causes no significant effect at the early stages of interdiffusion with 316L stainless steel*.

At 1123 K, as visible on EDS profile in Fig. 9-b, the phases sequence near the interface is qualitatively the same as that observed in bulk diffusion couples, with quantitative differences suggesting the onset of diverging mechanisms. Samples surface corresponds to non-transformed α-Ti. Thickness reduction to 450 nm (from initial 1300 nm titanium coating) is incompatible with the small measured increase of oxygen contents (30 at. % in Fig. 9-b). Contrary to bulk samples, *oxygen rejection during α-to-β phase transformation is not complete, owing to higher oxygen concentration in titanium coatings*. Next, a 250 nm β-Ti layer contains 12 at. % iron and 16 at. % oxygen. Fe diffusion in titanium coatings is much shallower than for bulk materials (15 μm deep). Residual oxygen in β-Ti and slowed iron diffusion seem to indicate that *α-to-β phase transformation front is controlled by thermodynamic stability and oxygen partitioning between the phases*. While no bibliographic data is available for Fe–Ti–O ternary system, these observations also prove that *some solubility in iron-enriched β-titanium exists for high enough oxygen activity* (somewhere between 10 and 30 at. %). A 700 nm FeTi layer contains 6 at. % oxygen. Similarly to the previous layer, *some small oxygen solubility in FeTi compound exists for high oxygen activity*. A dark spots pattern is visible on SEM images (Fig. 9-b). Contrary to bulk diffusion samples, these structures are not correlated to increased carbon concentration and thus do not correspond to TiC phase formation. Consequently, carbon diffusion into the interface appears to be linked and proportional to iron diffusion through it, possibly as a result of rising defects generated by Kirkendall effect.

The summed thicknesses of these three layers correspond to the initial titanium coating, confirming that *intermetallics compounds grow in the same directions as for bulk samples*: FeTi inside titanium and Fe_2Ti inside steel.

Progressing into 316L, the Fe_2Ti layer (100 nm thick) is mostly the same in composition and size as seen in bulk diffusion couples. A final chromium-enriched ferrite layer is also present, smaller than its equivalent formed in bulk materials (350 nm against 500 nm, respectively). The difference is not proportional to the amount of iron and nickel diffusing trough the interface during their respective thermal cycles, confirming that the size of this phase is controlled by a dynamic balance of the diffusing elements.

Microstructures formed at 1223 K show less defined borders and etching irregularities and, as a consequence, are more difficult to delimitate through SEM imaging alone (Fig. 9-c). Phase identification relied mostly on EDS profiles (Fig. 9-c), leading to some spatial resolution loss. Since diverging evolution from bulk diffusion couples has already been evidenced at lower temperature, structural descriptions will concentrate on elucidating formation mechanisms and phases specific to coated diffusion couples. The outermost layer (500 nm thick on Fig. 9-c) presents a smooth aspect and a few darker spots corresponding to localized etching. This layer contains mostly oxygen and titanium in equal proportions, which, together with electrical charges accumulation during SEM imaging, *indicates phase change to covalent titanium oxide TiO*. Transformation is probably triggered by partial oxygen rejection at the iron diffusion front, leading to oxygen progressively concentrating as α-Ti thickness decreases. Spots are correlated with lower local oxygen contents (<35 at. %, overestimated due to neighboring TiO matrix), and could correspond to residual α-titanium. No β-Ti layer remains at this temperature, the result of iron diffusion being inhibited by rising oxygen contents in α-Ti and FeTi growth completely replacing β-Ti. Molybdenum segregation (around 4 at. % - three times higher than in 316L) at the outer surface (<100 nm) is a common behavior observed in various oxides [71,77,78]. FeTi layer grows to 1100 nm, leaving no trace of transformed β-Ti. Oxygen contents are similar to those observed at 1123 K (6 at. %). Increased nickel concentration to 6 at. % is identical to what is measured in bulk diffusion couples under the same experimental conditions, while iron diffusion in titanium is much slower. *These observations could confirm that composition changes are related to improved thermodynamic stability, indicating a shift from kinetics-controlled growth happening at lower temperatures*. SEM images (Fig. 9-c) evidence a spots pattern similar to the structures visible at 1123 K. SEM-EDS profiles (Fig. 9-c) confirm local composition to be compatible with TiO oxide (area indicated by an arrow on the right side of composition profile in Fig. 9-c). The gradient of increasing spots density and diameters towards the surface indicates a dependency to oxygen contents in neighboring titanium. The most probable formation mechanism involves a slowed diffusion of iron in titanium with increasing oxygen presence. The resulting lateral diffusion of iron (with simultaneous Ti α-to-β transformation) then traps α-Ti oxygen-enriched inclusions in an iron-enriched β-Ti matrix. This structure is significantly different from the percolating α-Ti network visible in bulk diffusion couples, the latter allowing progressive oxygen rejection/elimination. The volume reduction of the inclusions leads to oxygen concentrating, and their eventual transformation to TiO oxide. This mechanism also explains the instabilities of the iron diffusion front observed in sputtered titanium. Finally, *oxygen maximum solubility in FeTi intermetallic compound can be estimated at 6 at %*.

Total thickness of these first two layers is 1600 nm, more than initial titanium coating (1300 nm). The difference can be ascribed to the 50% volume expansion occurring during oxide formation (as estimated from titanium compounds density data [79]).

Fe_2Ti layer (200 nm thick) shows a homogeneously smooth aspect. This phase is essentially stable (its low formation enthalpy is confirmed by Gasior et al. [60]), and its growth is probably further inhibited by the neighboring ferrite. The ferrite layer is thinner than the one formed in the bulk couples (600 nm against 950 nm, respectively), with similar titanium concentration (around 5 at. %). Chromium fraction (30 at. %) is identical to bulk samples and generally independent from the heat treatment temperature.

Darker spots in ferrite and into a small neighboring depth (500 nm) of 316L stainless steel are correlated with an increased titanium and decreased iron concentrations (27 at. % Ti, and 39 at. % Fe respectively, from Fig. 9-c). Considering chromium presence (19 at. %) and its capability to substitute iron in intermetallics (Supplementary Table 1), *these structures can be identified as Fe_2Ti compound* $(Fe_{1.3}Cr_{0.7})Ti$ more precisely). Titanium amounts (measured at 20 kV) at the boundary between ferrite and austenite depend on experimental conditions: 2 at. % for bulk samples, and 4–5 at. % for Ti coatings. These observations reveal a *deeper titanium diffusion in non-transformed 316L compared to bulk diffusion couples*, explaining the additional nucleation of titanium intermetallic compounds in Ti-saturated ferrite and austenite (Arrow on the left of profile in Fig. 9-c). Two (non-exclusive) mechanisms could elucidate such phenomenon: the first possibility is that titanium is trapped as intermetallics. Indeed, Ti diffuses into and reacts with stainless steel, forming Fe_2Ti. As this compound is thinner (50 nm less than bulk couples) in coated samples, more titanium is released in 316L. Considering the limited titanium amounts involved during Fe_2Ti formation, this model is unlikely to account for the whole titanium measured in 316L (both solid solution and nucleated intermetallics) in the case of coated couples. The second possibility is that the ferrite layer acts as a storage for titanium diffusing through the interface. Due to its higher solubility in ferrite (5 at. % according to Supplementary Table 1), titanium progression in stainless steel is impossible until complete saturation of the ferrite layer is reached. In the case of diffusion in coated couples, ferrite formation is more limited (600 nm instead of 950 nm), and titanium saturation is consequently more quickly reached, this element overflowing into austenite. Under this hypothesis, the limited diffusion of Ti into ferrite layer evidenced for bulk samples can be seen as a coincidence, since the titanium amount released on 316L side and the transformed ferrite thickness (demonstrated to be determined by a dynamic nickel and iron diffusion balance) are not directly related by a common mechanism.

5. Conclusions and perspectives

As a way to better understand and optimize hybrid processes for titanium coated stainless steel carburization, increasingly complex diffusion couples (bulk Fe/Ti, bulk 316L/Ti, and sputtered Ti on 316L) have been prepared and analyzed by coupled microstructural (SEM, TEM) and chemical (STEM-EDS, SEM-EDS) characterization methods. Comparison between Fe/Ti and 316L/Ti bulk diffusion couples allowed to precisely describe their microstructural and chemical characteristics, propose evolution mechanisms, and elucidate the early stages of such joinings formation. The variety of formed phases reported in former works can be mainly ascribed to species filtering and capturing mechanisms taking place in Fe/Ti intermetallics, as well as the transitory existence of some compounds.

During initial contact, intermetallics that will be the basis for FeTi and Fe_2Ti growth start to form at the junction between materials. Fast, Ti-β-stabilizing elements (Ni, Fe) diffuse as smooth successive fronts and trigger α-to-β transformation in titanium. Chromium diffusion is blocked by interfacial intermetallics. This obstruction causes local nickel and iron depletion to trigger austenite to ferrite transformation on 316L side. Increased solubility in ferrite delays titanium diffusion into steel until saturation.

During the following kinetics-controlled stage, a duplex α/β gradient structure is created in titanium by the interplay of oxygen (α-stabilizer) and long-range diffusion of iron (β-stabilizer). Morphology is controlled by Fe and O diffusion kinetics rather than thermodynamic stability. FeTi intermetallic compound grows from the interface into titanium. This compound acts as a perfect filter for carbon, trapping this element as TiC particles. Iron and carbon diffusions through the interface appear coupled. Fe_2Ti intermetallic compound grows from the interface into stainless steel. Intermetallics thicknesses are determined by the formation kinetics of each compound instead of the elements diffusion kinetics. Ferrite layer thickness is controlled by the dynamic diffusion balance existing between iron depletion into titanium and its supply from untransformed 316L

During the final transition towards a thermodynamics-controlled stage, structures remain similar but undergo composition changes to minimize energy. Iron is partially substituted by nickel and chromium in FeTi compound and partially substituted by chromium in Fe_2Ti compound. Further iron depletion from ferrite leads to an increase in chromium concentration and triggers sigma-phase (FeCr) nucleation, which will eventually grow to replace its parent phase.

Further comparisons with diffusion couples involving PVD coatings showed similar, but less defined, interfacial structures. The observed differences could all be directly related to titanium thickness, with no evaluable effect of the coating itself. Limited iron diffusion depth in titanium leads to smaller interfacial structures, proportionally farther Ti diffusion in 316L and ferrite, and subsequent additional Fe_2Ti nucleation. Oxygen rejection from iron diffusion front leads to increasing solid solution concentration inside α-Ti. The consequences are geometrically unstable boundaries, as well as oxide (TiO) formation, both on coating surface and as discrete inclusions.

Finally, some phases (β-Ti and FeTi) have been demonstrated to allow previously unreported solubility under high oxygen activity, reaching 6 at. % in β-titanium and 16 at. % in FeTi intermetallic compound.

Funding

This work was supported by Bourgogne-Franche-Comté Region France [project number 2020Y-19371]; and European Regional Development Fund [reference PO FEDER-FSE Bourgogne 2014–2020].

CRediT authorship contribution statement

J.-M. Auger: Conceptualization, Methodology, Validation, Investigation, Resources, Writing – original draft, Writing – review & editing, Visualization, Supervision. **D. Cotton:** Conceptualization, Methodology, Validation, Investigation, Resources, Writing – original draft, Writing – review & editing, Visualization, Supervision, Project administration, Funding acquisition. **C. Nouveau:** Conceptualization, Methodology, Validation, Investigation, Resources, Writing – original draft, Writing – review & editing, Visualization, Supervision, Project administration, Funding acquisition. **A. Besnard:** Conceptualization, Methodology, Validation, Investigation, Resources, Writing – original draft, Writing – review & editing, Visualization, Supervision, Project administration, Funding acquisition. **F. Bernard:** Conceptualization, Methodology, Validation, Investigation, Resources, Writing – original draft, Writing – review & editing, Visualization, Supervision, Project administration, Funding acquisition. **M.-R. Ardigo-Besnard:** Conceptualization, Methodology, Validation, Investigation, Resources, Writing – original draft, Writing – review & editing, Visualization, Supervision, Project administration, Funding acquisition. **J.-P. Monchoux:** Conceptualization, Methodology, Validation, Investigation, Resources, Writing – original draft, Writing – review & editing, Visualization, Supervision. **R. Cours:** Conceptualization, Methodology, Validation, Investigation, Resources, Writing – original draft, Writing – review & editing, Visualization, Supervision. **C. Marcelot:** Conceptualization, Methodology, Validation, Investigation, Resources, Writing – original draft, Writing – review & editing, Visualization, Supervision.

Declaration of competing interest

The authors declare that they have no known competing financial interests or personal relationships that could have appeared to influence the work reported in this paper.

Data availability

Data will be made available on request.

Acknowledgments

This work has been realized in the framework of the THEMPO project. The authors wish to thank the Bourgogne-Franche-Comté Region (project number 2020Y-19371) and the European Regional Development Fund (reference: PO FEDER-FSE Bourgogne 2014–2020) for their financial support. The authors also thank the doctoral school SMI 432 of Arts et Metiers Institute of Technology for the twenty months postdoctoral position.

Appendix A. Supplementary data

Supplementary data to this article can be found online at https://doi.org/10.1016/j.matchemphys.2023.128013.

References

[1] P.C. Van Wiggen, H.C.F. Rozendaal, E.J. Mittemeijer, The nitriding behaviour of iron-chromium-carbon alloys, J. Mater. Sci. 20 (1985) 4561–4582, https://doi.org/10.1007/BF00559347.

[2] J.I. Goldstein, A.E. Moren, Diffusion modeling of the carburization process, Metall. Mater. Trans. A 9 (1978) 1515–1525, https://doi.org/10.1007/BF02661934.

[3] M. Kobayashi, T. Matsui, Y. Murakami, Mechanism of creation of compressive residual stress by shot peening, Int. J. Fatig. 20 (1998) 351–357, https://doi.org/10.1016/S0142-1123(98)00002-4.

[4] W. Deqing, S. Ziyuan, Z. Longjiang, A liquid aluminum corrosion resistance surface on steel substrate, Appl. Surf. Sci. 214 (2003) 304–311, https://doi.org/10.1016/S0169-4332(03)00505-1.

[5] L. De Schepper, M. D'Olieslaeger, G. Knuyt, L.M. Stals, M. Van Stappen, B. Malliet, J.P. Celis, J.R. Roos, Initial growth and epitaxy of PVD TiN layers on austenitic steel, Thin Solid Films 173 (1989) 199–208, https://doi.org/10.1016/0040-6090(89)90135-1.

[6] A. Derre, M. Ducarroir, F. Teyssandier, Deposition parameters controlling CVD of TiC on steel, J. Electrochem. Soc. 136 (1989) 853, https://doi.org/10.1149/1.2096756.

[7] R. Vilar, Laser cladding, J. Laser Appl. 11 (1999) 64–79, https://doi.org/10.2351/1.521888.

[8] S. Yang, K. Cooke, H. Sun, X. Li, K. Lin, H. Dong, Development of advanced duplex surface systems by combining CrAlN multilayer coatings with plasma nitrided steel substrates, Surf. Coating. Technol. 236 (2013) 2–7, https://doi.org/10.1016/j.surfcoat.2013.07.017.

[9] G. Cassar, S. Banfield, J.C.A.-B. Wilson, J. Housden, A. Matthews, A. Leyland, Tribological properties of duplex plasma oxidised, nitrided and PVD coated Ti–6Al–4V, Surf. Coating. Technol. 206 (2011) 395–404, https://doi.org/10.1016/j.surfcoat.2011.07.037.

[10] A.F. Rousseau, J.G. Partridge, E.L.H. Mayes, J.T. Toton, M. Kracica, D. G. McCulloch, E.D. Doyle, Microstructural and tribological characterisation of a nitriding/TiAlN PVD coating duplex treatment applied to M2 High Speed Steel tools, Surf. Coating. Technol. 272 (2015) 403–408, https://doi.org/10.1016/j.surfcoat.2015.03.034.

[11] M. Song, J. Guo, Y. Yang, K. Geng, M. Xiang, Q. Zhu, C. Hu, H. Zhao, Fe_2Ti interlayer for improved adhesion strength and corrosion resistance of TiN coating on stainless steel 316L, Appl. Surf. Sci. 504 (2020), 144483, https://doi.org/10.1016/j.apsusc.2019.144483.

[12] H.J. Boving, H.E. Hintermann, Wear-resistant hard titanium carbide coatings for space applications, Tribol. Int. 23 (1990) 129–133, https://doi.org/10.1016/0301-679X(90)90045-Q.

[13] T. Jamal, R. Nimmagadda, R.F. Bunshah, Friction and adhesive wear of titanium carbide and titanium nitride overlay coatings, Thin Solid Films 73 (1980) 245–254, https://doi.org/10.1016/0040-6090(80)90487-3.

[14] D. Hong, Y. Niu, H. Li, X. Zhong, W. Tu, X. Zheng, J. Sun, Comparison of microstructure and tribological properties of plasma-sprayed TiN, TiC and TiB2 coatings, Surf. Coating. Technol. 374 (2019) 181–188, https://doi.org/10.1016/j.surfcoat.2019.05.071.

[15] D.B. Miracle, H.A. Lipsitt, Mechanical properties of fine-grained substoichiomebic titanium carbide, J. Am. Ceram. Soc. 66 (1983) 592–597, https://doi.org/10.1111/j.1151-2916.1983.tb10098.x.

[16] J. Musil, P. Baroch, J. Vlček, K.H. Nam, J.G. Han, Reactive magnetron sputtering of thin films: present status and trends, Thin Solid Films 475 (2005) 208–218, https://doi.org/10.1016/j.tsf.2004.07.041.

[17] M. Zaludová, B. Smetana, S. Zlá, J. Dobrovskâ, V. Vodárek, K. Konečná, V. Matějka, P. Matějková, Experimental study of Fe–C–O based system below 1000 °C, J. Therm. Anal. Calorim. (2012), https://doi.org/10.1007/s10973-012-2346-y.

[18] C. Leyens, M. Peters, Titanium and Titanium Alloys: Fundamentals and Applications, 2003, https://doi.org/10.1002/3527602119.

[19] H. Nakajima, M. Koiwa, Diffusion of iron, cobalt and nickel in alpha-titanium, Titanium–Sci. Technol. 3 (1984) 1759–1766.

[20] J.L. Murray, H.A. Wriedt, The O-Ti (Oxygen-Titanium) system, J. Phase Equil. 8 (1987) 148–165, https://doi.org/10.1007/BF02873201.

[21] H. Nakajima, M. Koiwa, Diffusion in titanium, ISIJ Int. 31 (1991) 757–766, https://doi.org/10.2355/isijinternational.31.757.

[22] R.F. Peart, D.H. Tomlin, Diffusion of solute elements in beta-titanium, Acta Metall. 10 (1962) 123–134, https://doi.org/10.1016/0001-6160(62)90057-3.

[23] T. Haure, Couches Multifonctionnelles Par Procédé Multitechnique = Multifunctional Alumina Deposits Obtained by Combining Two Dry Processes, Limoges, 2003. http://aurore.unilim.fr/ori-oai-search/notice/view/unilim-ori-12917. (Accessed 7 March 2022).

[24] T.P.S. Gill, M. Vijayalkshmi, P. Rodriguez, K.A. Padmanabhan, On microstructure-property correlation of thermally aged type 316L stainless steel weld metal, Metall. Mater. Trans. A 20 (1989) 1115–1124, https://doi.org/10.1007/BF02650146.

[25] J.X. Zou, K.M. Zhang, T. Grosdidier, C. Dong, Y. Qin, S.Z. Hao, D.Z. Yang, Orientation-dependent deformation on 316L stainless steel induced by high-current pulsed electron beam irradiation, Mater. Sci. Eng., A 483–484 (2008) 302–305, https://doi.org/10.1016/j.msea.2006.07.179.

[26] W.-S. Lee, C.-F. Lin, Impact properties and microstructure evolution of 304L stainless steel, Mater. Sci. Eng., A 308 (2001) 124–135, https://doi.org/10.1016/S0921-5093(00)02024-4.

[27] A. Szymaska, D. Oleszak, A. Grabias, M. Rosiński, K. Sikorski, J. Kazior, A. Michalski, K.J. Kurzydłowski, Phase transformations in ball milled AISI 316L stainless steel powder and the microstructure of the steel obtained by its sintering, Rev. Adv. Mater. Sci. 8 (2004) 143–146.

[28] R. Song, J. Xiang, D. Hou, Characteristics of mechanical properties and microstructure for 316L austenitic stainless steel, J. Iron Steel Res. Int. 18 (2011) 53–59, https://doi.org/10.1016/S1006-706X(11)60117-9.

[29] P. Dhaiveegan, N. Elangovan, T. Nishimura, N. Rajendran, Corrosion behavior of 316L and 304 stainless steels exposed to industrial-marine-urban environment: field study, RSC Adv. 6 (2016) 47314–47324, https://doi.org/10.1039/C6RA04015B.

[30] J. Liebertz, S. Stähr, S. Haussühl, Growth and properties of single crystals of FeTi, Krist. Tech. 15 (1980) 1257–1260, https://doi.org/10.1002/crat.19800151105.

[31] D. Chanbi, L. Adnane Amara, E. Ogam, S. Amara, Z. Fellah, Microstructural and mechanical properties of binary Ti-rich Fe–Ti, Al-rich Fe–Al, and Ti–Al alloys, Materials 12 (2019) 433, https://doi.org/10.3390/ma12030433.

[32] G.D. Sandrock, J.J. Reilly, J.R. Johnson, Metallurgical Considerations in the Production and Use of FeTi Alloys for Hydrogen Storage, Brookhaven National Lab., Upton, N.Y. (USA), 1976. https://www.osti.gov/biblio/7341735. (Accessed 17 September 2021).

[33] W. Li, L. Yan, S. Karnati, F. Liou, J. Newkirk, K.M.B. Taminger, W.J. Seufzer, Ti-Fe intermetallics analysis and control in joining titanium alloy and stainless steel by Laser Metal Deposition, J. Mater. Process. Technol. 242 (2017) 39–48, https://doi.org/10.1016/j.jmatprotec.2016.11.010.

[34] K.D. Ciricć, A. Kocjan, A. Gradišek, V.J. Koteski, A.M. Kalijadis, V.N. Ivanovski, Z. V. Laušević, D.Lj Stojić, A study on crystal structure, bonding and hydriding properties of Ti-Fe-Ni intermetallics - behind substitution of iron by nickel, Int. J. Hydrogen Energy 37 (2012) 8408–8417, https://doi.org/10.1016/j.ijhydene.2012.02.047.

[35] T. Suda, M. Ohkawa, S. Sawada, S. Watanabe, S. Ohnuki, S. Nagata, Effect of surface modification by ion implantation on hydrogenation property of TiFe alloy, Mater. Trans. 43 (2002) 2703–2705, https://doi.org/10.2320/matertrans.43.2703.

[36] T. Suzuki, S. Uehara, Mechanical properties of FeTi, CoTi, and NiTi at elevated temperatures, Titanium 2 (1980) 1255–1263.

[37] S. Wang, K. Wang, G. Chen, Z. Li, Z. Qin, X. Lu, C. Li, Thermodynamic modeling of Ti-Fe-Cr ternary system, Calphad 56 (2017) 160–168, https://doi.org/10.1016/j.calphad.2016.12.007.

[38] D. Dew-Hughes, L. Kaufman, Ternary phase diagrams of the manganese-titanium-iron and the aluminum-titanium-iron systems: a comparison of computer calculations with experiment, Calphad 3 (1979) 175–203, https://doi.org/10.1016/0364-5916(79)90003-8.

[39] G. Cacciamani, J. De Keyzer, R. Ferro, U.E. Klotz, J. Lacaze, P. Wollants, Critical evaluation of the Fe–Ni, Fe–Ti and Fe–Ni–Ti alloy systems, Intermetallics 14 (2006) 1312–1325, https://doi.org/10.1016/j.intermet.2005.11.028.

[40] A.J. Knowles, N.G. Jones, C.N. Jones, H.J. Stone, Phase equilibria in the Fe-Mo-Ti ternary system at 1173 K (900 °C) and 1023 K (750 °C), Metall. Mater. Trans. A 48 (2017) 4334–4341, https://doi.org/10.1007/s11661-017-4134-6.

[41] V.P. Shapovalov, A.N. Kurasov, Diffusion of titanium in iron, Met. Sci. Heat Treat. 17 (1975) 803–805, https://doi.org/10.1007/BF00703075.

[42] G. Requena, K. Bugelnig, F. Sket, S. Milenkovic, G. Rödler, A. Weisheit, J. Gussone, J. Haubrich, P. Barriobero-Vila, T. Pusztai, L. Gránásy, A. Theofilatos, J.C. da Silva, U. Hecht, Ultrafine Fe-Fe2Ti eutectics by directed energy deposition: insights into microstructure formation based on experimental techniques and phase field modelling, Addit. Manuf. 33 (2020), 101133, https://doi.org/10.1016/j.addma.2020.101133.

[43] A. Shamsolhodaei, J.P. Oliveira, N. Schell, E. Maawad, B. Panton, Y.N. Zhou, Controlling intermetallic compounds formation during laser welding of NiTi to 316L stainless steel, Intermetallics 116 (2020), 106656, https://doi.org/10.1016/j.intermet.2019.106656.

[44] M.C.J. Marker, L.I. Duarte, C. Leinenbach, K.W. Richter, Characterization of the Fe-rich corner of Al-Fe-Si-Ti, Intermetallics 39 (2013) 38–49, https://doi.org/10.1016/j.intermet.2013.03.007.

[45] T. Li, D. Zhou, Y. Yan, P. Peng, J. Liu, First-principles and experimental investigations on ductility/brittleness of intermetallic compounds and joint properties in steel/aluminum laser welding, Trans. Nonferrous Metals Soc. China 31 (2021) 2962–2977, https://doi.org/10.1016/S1003-6326(21)65706-0.

[46] V. Ivanchenko, T. Pryadko, G. Effenberg, S. Ilyenko, Ternary Alloy Systems: Phase Diagrams, Crystallographic and Thermodynamic Data Critically Evaluated by MSIT® · Iron Systems Part 2: Selected Systems from Al-B-Fe to C-Co-Fe, Springer-Verlag Berlin and Heidelberg GmbH & Co. K, 2008, https://doi.org/10.1007/978-3-540-74196-1.

[47] W. Zheng, W. Song, T. Wu, J. Wang, Y. He, X.-G. Lu, Experimental investigation and thermodynamic modeling of the ternary Ti–Fe–Mn system for hydrogen storage applications, J. Alloys Compd. 891 (2022), 161957, https://doi.org/10.1016/j.jallcom.2021.161957.

[48] T.B. Massalski, H. Okamoto, Binary Alloy Phase Diagrams, second ed., ASM International, Materials Park, Ohio, 1990.

[49] V.B. Vykhodets, S.M. Klotsman, T.E. Kurennykh, L.D. Kurmaeva, A.D. Levin, Oxygen diffusion in alpha Ti. I. Anisotropy of oxygen diffusion in alpha Ti, Fiz. Met. Metalloved. (1987) 63. https://www.osti.gov/etdeweb/biblio/5741894. (Accessed 8 April 2022).

[50] R.A. Perez, F. Dyment, H. Nakajima, Diffusion in α-Ti and Zr, Mater. Trans., JIM 44 (2003) 2–13, https://doi.org/10.2320/matertrans.44.2.

[51] D. Poddar, Solid-state diffusion bonding of commercially pure titanium and precipitation hardening stainless steel, Int. J. Recent Trends Eng. 1 (2009) 93.

[52] Y.M. Mishin, 50 Years of grain boundary diffusion: what do we know about it today? Defect Diffusion Forum 194–199 (2001) 1113–1126. https://doi.org/10.4028/www.scientific.net/DDF.194-199.1113.

[53] C. Herzig, S. Divinski, Y. Mishin, Bulk and interface boundary diffusion in group IV hexagonal close-packed metals and alloys, Metall. Mater. Trans. A 33 (2002) 765–775, https://doi.org/10.1007/s11661-002-0143-0.

[54] D.A. Aksyonov, A.G. Lipnitskii, Solubility and grain boundary segregation of iron in hcp titanium: a computational study, Comput. Mater. Sci. 137 (2017) 266–272, https://doi.org/10.1016/j.commatsci.2017.05.034.

[55] H. Bo, J. Wang, L. Duarte, C. Leinenbach, L. Liu, H. Liu, Z. Jin, Thermodynamic re-assessment of Fe–Ti binary system, Trans. Nonferrous Metals Soc. China 22 (2012) 2204–2211, https://doi.org/10.1016/S1003-6326(11)61450-7.

[56] K. Hirano, Y. Ipposhi, Interdiffusion in Fe-Ti alloys, J. Jpn. Inst. Metals 32 (1968) 815–821, https://doi.org/10.2320/jinstmet1952.32.9_815.

[57] M. Carbucicchio, G. Palombarini, On the interface between iron and thin films of titanium and titanium nitride, Hyperfine Interact. 57 (1990) 1783–1788, https://doi.org/10.1007/BF02405722.

[58] T. Chen, Z.L. Wu, B.S. Cao, J. Gao, M.K. Lei, Solid state reaction of Fe/Ti nanometer-scale multilayers, Surf. Coating. Technol. 201 (2007) 5059–5062, https://doi.org/10.1016/j.surfcoat.2006.07.150.

[59] A.M. Van der Kraan, K.H.J. Buschow, The 57Fe Mössbauer isomer shift in intermetallic compounds of iron, Phys. B+C 138 (1986) 55–62, https://doi.org/10.1016/0378-4363(86)90492-4.

[60] W. Gasior, A. Debski, Enthalpy of formation of intermetallic phases from Fe-Ni-Ti system, Compar. Stud., Arch. Metall. Mater. 57 (2012) 1095–1104.
[61] P. Bellen, K.C.H. Kumar, P. Wollants, Thermodynamic assessment of the Ni-Ti phase diagram, Int. J. Mater. Res. 87 (1996) 972–978, https://doi.org/10.1515/ijmr-1996-871207.
[62] P. Riani, G. Cacciamani, Y. Thebaut, J. Lacaze, Phase equilibria and phase transformations in the Ti-rich corner of the Fe–Ni–Ti system, Intermetallics 14 (2006) 1226–1230, https://doi.org/10.1016/j.intermet.2005.09.011.
[63] D. Mo, T. Song, Y. Fang, C. Luo, M. Simpson, Z. Luo, A review on diffusion bonding between titanium alloys and stainless steels, Adv. Mater. Sci. Eng. 2018 (2018) 1–15, https://doi.org/10.1155/2018/8701890.
[64] S.K. Ghosh, S. Chatterjee, On the direct diffusion bonding of titanium alloy to stainless steel, Mater. Manuf. Process. 25 (2010) 1317–1323, https://doi.org/10.1080/10426914.2010.520793.
[65] S. Kundu, S. Chatterjee, Diffusion bonding between commercially pure titanium and micro-duplex stainless steel, Mater. Sci. Eng. A-Struct. Mater. Prop. Microstruct. Proc. 480 (2008) 316–322, https://doi.org/10.1016/j.msea.2007.07.033.
[66] G.B. Kale, R.V. Patil, P.S. Gawade, Interdiffusion studies in titanium–304 stainless steel system, J. Nucl. Mater. 257 (1998) 44–50, https://doi.org/10.1016/S0022-3115(98)00179-2.
[67] S. Kundu, D. Roy, S. Chatterjee, D. Olson, B. Mishra, Influence of interface microstructure on the mechanical properties of titanium/17-4 PH stainless steel solid state diffusion bonded joints, Mater. Des. 37 (2012) 560–568, https://doi.org/10.1016/j.matdes.2011.10.041.
[68] A.A. Shirzadi, A. Laik, R. Tewari, J. Orsborn, G.K. Dey, Gallium-assisted diffusion bonding of stainless steel to titanium; microstructural evolution and bond strength, Materialia 4 (2018) 115–126, https://doi.org/10.1016/j.mtla.2018.09.009.
[69] M. Ghosh, K. Bhanumurthy, G.B. Kale, J. Krishnan, S. Chatterjee, Diffusion bonding of titanium to 304 stainless steel, J. Nucl. Mater. 322 (2003) 235–241, https://doi.org/10.1016/j.jnucmat.2003.07.004.
[70] G.F. Vander Voort, Metallography and Microstructures, ASM International, Materials Park, Ohio, 2004.
[71] L. Wang, A. Seyeux, P. Marcus, Thermal stability of the passive film formed on 316L stainless steel surface studied by ToF-SIMS, Corrosion Sci. 165 (2020), 108395, https://doi.org/10.1016/j.corsci.2019.108395.
[72] M.W. Chase, National Institute of Standards and Technology (U.S.), NIST-JANAF Thermochemical Tables, American Chemical Society ; American Institute of Physics for the National Institute of Standards and Technology, Washington, D.C.]; Woodbury, N.Y., 1998.
[73] Y. Yang, X. Zhang, Diffusion reaction in the interface of titanium/mild steel composite, J. Cent. South Univ. Technol. 3 (1996) 135–139, https://doi.org/10.1007/BF02652192.
[74] R. Feng, M.C. Gao, C. Zhang, W. Guo, J.D. Poplawsky, F. Zhang, J.A. Hawk, J. C. Neuefeind, Y. Ren, P.K. Liaw, Phase stability and transformation in a light-weight high-entropy alloy, Acta Mater. 146 (2018) 280–293, https://doi.org/10.1016/j.actamat.2017.12.061.
[75] A. Ben-Artzy, A. Reichardt, J.-P. Borgonia, R.P. Dillon, B. McEnerney, A.A. Shapiro, P. Hosemann, Compositionally graded SS316 to C300 Maraging steel using additive manufacturing, Mater. Des. 201 (2021), 109500, https://doi.org/10.1016/j.matdes.2021.109500.
[76] E.D. Boyes, Analytical potential of EDS at low voltages, Mikrochim. Acta 138 (2002) 225–234, https://doi.org/10.1007/s006040200026.
[77] Z.X. Liu, Y.Q. Li, S.X. Qi, K. Xie, N.J. Wu, Q.X. Bao, Segregation and chemical state of vanadium and molybdenum in vanadium—molybdenum oxide catalyst studied by x-ray photoelectron spectroscopy, Appl. Catal. 56 (1989) 207–218, https://doi.org/10.1016/S0166-9834(00)80170-0.
[78] P. Marcus, I. Olefjord, ESCA study of the oxidation of a nickel–molybdenum alloy, Surf. Interface Anal. 9 (1986) 377–381, https://doi.org/10.1002/sia.740090606.
[79] D.R. Lide, CRC Handbook of Chemistry and Physics, 89th Edition, 89e édition, CRC Press, Boca Raton, 2008.